

See discussions, stats, and author profiles for this publication at: <https://www.researchgate.net/publication/283241832>

Surrogate-based multi-point forming process optimization for dimpling and wrinkling reduction

Article in *The International Journal of Advanced Manufacturing Technology* · July 2016

DOI: 10.1007/s00170-015-7897-1

CITATIONS

30

READS

784

3 authors, including:



Misganaw Abebe

Pusan National University

9 PUBLICATIONS 74 CITATIONS

[SEE PROFILE](#)



Kyunghoon Lee

Pusan National University

1 PUBLICATION 30 CITATIONS

[SEE PROFILE](#)

Some of the authors of this publication are also working on these related projects:



Ship route optimization framework [View project](#)

Surrogate-based multi-point forming process optimization for dimpling and wrinkling reduction

Misganaw Abebe¹ · Kyunghoon Lee¹ · Beom-Soo Kang¹

Received: 22 May 2015 / Accepted: 24 September 2015 / Published online: 14 October 2015
© Springer-Verlag London 2015

Abstract Multi-point forming (MPF) has been gaining attention for use in flexible sheet metal forming, since it is conducive to the manufacture of various shapes. However, discrete punch elements may induce either dimples or wrinkles, resulting in defective products. To address these forming issues, this study aims to eliminate both dimpling and wrinkling by adjusting parameters such as the punch speed, punch pressure (cushion compressive strain ratio), and elastic cushion thickness through multi-objective optimization. Evaluation of dimpling and wrinkling under variation in these three MPF parameters benefits from ordinary Kriging for computational efficiency. Multi-objective optimization with a genetic algorithm is used to determine the Pareto fronts of the dimpling and wrinkling measures, and a technique for order preferences by similarity to ideal solution (TOPSIS) is performed for identifying the best candidate among the Pareto optima. Finally, a dimpling-and-wrinkling-free TOPSIS solution is numerically verified by comparison with results of a full model simulation and experimentally validated by its application to a manufactured product.

Keywords Multi-point forming · Dimpling · Wrinkling · Pareto front · Technique for order preferences by similarity to ideal solution · Ordinary Kriging

✉ Beom-Soo Kang
bskang@pusan.ac.kr

Misganaw Abebe
misge98@gmail.com

Kyunghoon Lee
aeronova@pusan.ac.kr

¹ Department of Aerospace Engineering, Pusan National University, Busan 609-735, South Korea

Nomenclature

\mathbf{x}	inputs, process variables
y	outputs, response of interest in Kriging
r	punch tip radius
t_b	blank thickness
t_c	cushion thickness
u_f	node displacement after deformation
u	target surface node displacement
t_f	final blank thickness
t_o	initial blank thickness
c	compressive strain ratio of elastic cushion
L	blank length
P	punch width
R	curvature radius
W	blank width
ν	Poisson's ratio
ρ	density
ε_0	pre-strain or offset strain constant
ε	true plastic strain
σ	true stress
σ^2	variance
n	strain hardening exponent
θ_l	l^{th} Kriging hyperparameter
μ	constant global trend
C_{01}	material constant
C_{10}	material constant
E	expectation
\bar{I}_1	first deviatoric strain invariant
\bar{I}_1	first deviatoric strain invariant
\bar{I}_2	second deviatoric strain invariant
K	strength coefficient
N	total number of nodes
N_e	total number of elements
p_l	correlation function smoothness

- Ω sample space
- ψ correlation function
- Ψ correlation matrix
- U strain energy per unit of reference volume

1 Introduction

Multi-point forming is one of the various available techniques for flexible metal forming employs a discrete hemispherical punch for multi-curvature forming. The main advantage of multi-point forming (MPF) attributes to the fact that it is easy to reconfigure a punch array for diverse geometries. Since the establishment of a reconfigurable discrete die by installing punches on a numerically controlled milling machine headstock by Nakajima [1], the forming mechanism has been extended to processes such as stamping and stretch forming. For instance, Valjavec and Hardt [2] proposed a closed-loop shape control of the stretch forming process over a reconfigurable tool for precision airframe skin fabrication, and Park et al. [3] performed numerical and experimental investigations of the stretching effect on flexible forming. Similarly, researchers in the field of stamping have devised various methods such as sectional MPF [4], multi-point press forming [1], and iterative (MPF) [4]. Various rapid yet cost-effective techniques [5] have also been proposed for improvement of the multi-point pressure forming process. Such techniques have been applied to many different products, such as a ship hull plate [6] and aircraft body panel [7].

Despite the aforementioned utility of MPF, an MPF-processed product is prone to defects such as dimples and wrinkles. During MPF, dimples are induced by point contacts between the respective punch ends and the sheet plate, and wrinkles are induced because of compressive instability. As reported in a previous study [8], the initiation and growth of wrinkling are affected by a number of factors such as stress, strain, material properties, the workpiece geometry, and contact conditions. For elimination of wrinkles in stamp forming, the punch pressure should be greater than the induced compressive force in the sheet blank. However, the increase in punch pressure conversely tends to cause dimples in MPF due to the discrete punch elements.

As a solution to overcome these drawbacks, the use of an elastic cushion has been proposed and adopted for absorbing external energy resulting from excessive punch pressure [9]. To determine an appropriate cushion thickness and punch pressure depending on the material, researchers have performed a numerical investigation using simulation and subsequent validation via physical experiments. For example, Quan et al. [10] tested different cushion thicknesses numerical simulation to improve the formability of AZ31B sheet metal by determining an appropriate elastic cushion thickness. Cai et al. [11] performed numerical investigations

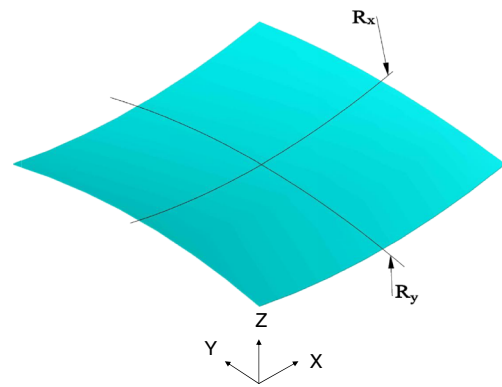


Fig. 1 Target saddle shape

of wrinkling, dimpling, and springback in MPF for various blank thicknesses, punch forces, and curvature radii. Zhang et al. [12] performed numerical simulation for investigating the deformation of a sheet in multi-point sandwich forming. Nevertheless, numerical investigation with high-fidelity simulation, such as finite element (FE) simulation, is time consuming and resource demanding so that finding dimpling-and-wrinkling-free MPF parameters becomes formidable. Therefore, the present study addresses the problem of determining the best MPF parameters by employing multi-objective optimization along with surrogate modeling for achieving computational effectiveness.

Surrogate models replace the expensive FE analysis approach and considerably shorten the development time in the early design stages. Some researchers employed a surrogate model of sheet metal forming. For example, Liu et al. [13] applied polynomial fitting for examining the effects of the cushion material, cushion thickness, and the coefficient of friction on the surface quality of the deformed sheet. Wessing et al. [14] employed Kriging and artificial neural networks to predict the thickness distribution of cold-formed B-pillars in comparison with experimental results. Sun et al. [15] proposed a new multi-objective optimization algorithm called multi-objective particle swarm optimization and employed radial basis functions for constructing meta-models for fracture and wrinkling criteria in sheet metal forming design. Xia et al. [16] introduced Gaussian process simultaneous model for optimizing the process parameters and improving the quality control for multi-objective optimization problems of sheet metal forming. In die stamping, other meta-modeling techniques, such as space mapping [17], radial base function networks [18], a simplified inverse approach [19], and response surface methodology [20] were employed for the optimum design of sheet metal forming parts. However, these techniques were applied to single die forming.

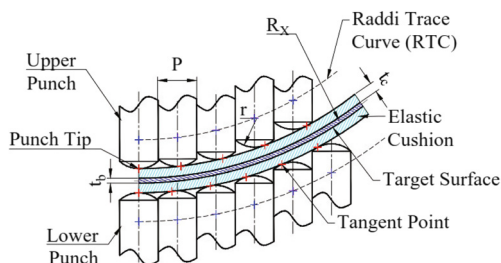
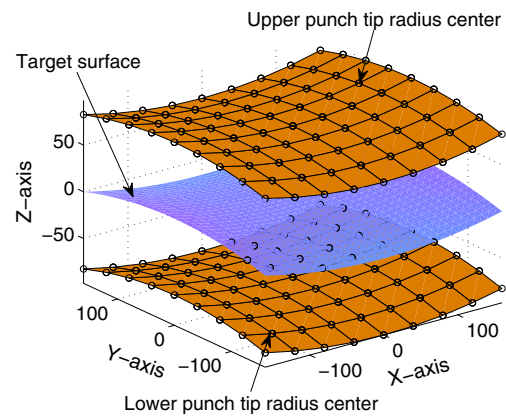
This study proposes multi-objective optimization along with surrogate modeling with the aim of reducing both

Table 1 Material properties of AA3003-H14

Properties	Value	Unit
Young's modulus	70.1	GPa
Poisson's ratio	0.33	N/A
Density	2700	kg/m ²
Yield stress	152.2	MPa
Strength coefficient	192.7	MPa
Pre-strain constant	2.51×10^{-3}	N/A
Strain hardening exponent	0.0394	N/A

wrinkling and dimpling in the forming of a saddle shape by MPF with consideration of three influencing parameters: the punch speed, cushion compressive strain ratio, and cushion thickness. First, Kriging surrogate model was applied to replace the FE analysis that would reduce the computational time. Second, multi-objective optimization with the genetic algorithm in MATLAB was employed to determine the Pareto front for wrinkling and dimpling measures with the aim of establishing the best candidate for the MPF parameters. Finally, the technique for order preferences by similarity to ideal solution (TOPSIS) was applied to determine the optimum combination of the parameters from the Pareto front. The dimpling-and-wrinkling-free TOPSIS solution was numerically verified by comparison with the results of a numerical simulation and validated experimentally by comparison with experimental results.

The rest of this paper is organized as follows. Section 2 presents the geometry model, the material model, and the simulation model for the MPF of a saddle shape. Section 3 describes the sampling design, the formulation of ordinary kriging interpolation, and the verification of Kriging surrogates with respect to the FE model. Section 4 presents optimal MPF parameters for reduction of dimpling and wrinkling as Pareto fronts, identification of the best candidates by TOPSIS for different scenarios, and the experimental validation of the numerical results.

**Fig. 2** Two-dimensional view of arrangement of MPF punch**Fig. 3** Upper and lower hemispherical punch-tip center traced surface

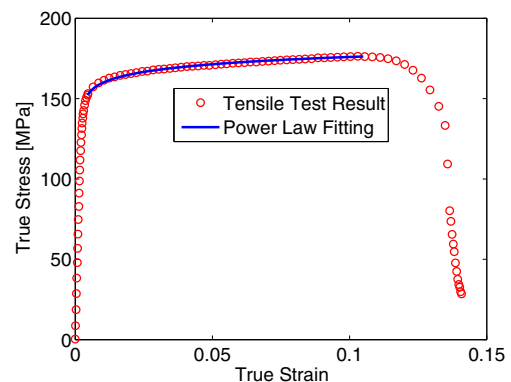
2 Finite element modeling

2.1 Geometry model

The target geometry for this study is a rectangular saddle shape, as shown in Fig. 1. The shape equation can be derived from the spherical geometry: $R^2 = x^2 + y^2 + z^2$, where $R \in \mathbb{R}$ is the sphere radius, $x \in \mathbb{R}$, $y \in \mathbb{R}$, and $z \in \mathbb{R}$ are Cartesian coordinates. The saddle has two curvature radii; $R_x \in \mathbb{R}$ in the longitudinal direction (x -axis), and $R_y \in \mathbb{R}$ in the transverse direction (y -axis). For the yz -plane, the z -coordinate value is determined as $\sqrt{R_y^2 - y^2}$, and for the xz -plane, the z -coordinate value is determined as $\sqrt{R_x^2 - x^2}$. In Fig. 1, R_x is opens upward and R_y opens downward. Thus, the saddle shape equation is formulated as

$$Z(x, y) = \sqrt{R_y^2 - y^2} - \sqrt{R_x^2 - x^2}. \quad (1)$$

To acquire the target shape in MPF, the two axes x -axis and y -axis are fixed while the punch moves along the z -axis. The geometry of the punch is discretized by square grids of n nodes along the x -axis and of m nodes along the y -axis, where their pair (n, m) represents the center of a given

**Fig. 4** Trues stress-strain curve for AA3003-H14

hemispherical punch-tip. As shown in Fig. 2, the centers of the hemispherical upper- and lower-punch tips are traced by a curve termed radii trace curve (RTC). This curve is concentric with the target surface. The equidistance along the normal direction from the target surface is determined by $r + t_c + 0.5t_b$, which is obtained from the punch tip radius r , blank thickness t_b , and cushion thickness t_c . Based on Eq. 1, the corresponding positions of the upper and lower RTC surfaces are given as below in Eqs. 2 and 3, respectively.

$$Z_U(x_{ij}, y_{ij}) = \sqrt{(R_y^U)^2 - y_{ij}^2} - \sqrt{(R_x^U)^2 - x_{ij}^2}, \quad (2)$$

$$Z_L(x_{ij}, y_{ij}) = \sqrt{(R_y^L)^2 - y_{ij}^2} - \sqrt{(R_x^L)^2 - x_{ij}^2}, \quad (3)$$

where $0 < i < n$, $0 < j < m$. The curvature radius for the RTC surface of the upper punch in the longitudinal direction, R_x^U , is equal to $R_x - (r + t_c + 0.5t_b)$, and that in the transverse direction, R_y^U , is equal to $R_y + (r + t_c + 0.5t_b)$. For the lower punch, R_x^L is equal to $R_x + (r + t_c + 0.5t_b)$ and R_y^L is equal to $R_y - (r + t_c + 0.5t_b)$. Figure 3 presents the positions of the upper and lower RTC surfaces, obtained as a result of applying the proposed Eqs. 2 and 3, respectively.

2.2 Material model

The blank material used in this study is aluminum alloy AA3003-H14. A tensile test is performed to determine the significant material properties of AA3003-H14 for a 2-mm-thick sheet in the MTS machine, according to the ASTM - E8/E8M-13a standard. In this study, the deformation is assumed to be small so that the material can be treated as an isotropic material obeying Prandtl-Reuss flow rule and satisfies the Von-Mises yield criterion. An isotropic hardening model is employed for investigating the strain-hardening, and the material characteristics are denoted by the power law: $\sigma = K(\varepsilon_0 + \varepsilon)^n$ for $\sigma \geq \sigma_y$, where σ is the true stress, K is the strength coefficient, ε is the true plastic strain, ε_0 is the pre-strain or offset strain constant, and n is the

strain hardening exponent. Figure 4 shows the true stress-strain curve and the flow stress, obtained from the tensile test and power law fitting curve, respectively. The material properties are summarized in Table 1.

Polyurethane with a hardness of Shore 90A was chosen as the material of the elastic cushion; the material properties were taken from Heo et al. [21]. The Mooney-Rivlin hyper elastic material model was employed for describing the deformation behavior of the elastic cushion. The form of the Mooney-Rivlin energy potential is

$$U = C_{10}(\bar{I}_1 - 3) + C_{01}(\bar{I}_2 - 3), \quad (4)$$

where U is the strain energy per unit of reference volume, C_{10} and C_{01} are material constants, and \bar{I}_1 and \bar{I}_2 are the first and second deviatoric strain invariants, respectively. Figure 5 shows the curve of the nominal compressive stress vs. nominal compressive strain curve of the elastic cushion, as obtained from the uniaxial compression test; these data are applied to the Mooney-Rivlin model.

2.3 Simulation model

Multi-point forming is a complex mechanical process that includes non-linear geometry and boundary conditions, such as a discrete punch (discontinuous contact). For this study, dynamic explicit model was chosen to avoid the convergence problem and to improve the computational efficiency. ABAQUS commercial software was used for the numerical simulation with consideration of springback. As shown in Fig. 6, due to the symmetry of saddle-shape configurations, only a quarter of the part was considered. For the two symmetric sides of the sheet and cushions, symmetric boundary conditions were applied. Under x -symmetry, the translational displacement in the x -direction, and rotational in y -direction and z -direction were set to zero ($U_x = UR_y = UR_z = 0$), and under y -symmetry, translational displacement in y -direction, and rotation in x -direction and z -direction were set to zero ($U_y = UR_x = UR_z = 0$). The blank sheet was meshed with 6400 solid elements of the C3D8R type with 8 element nodes; the number of elements through the thickness was 2, and the total number of nodes was 13,122. One of the elastic cushions was meshed with

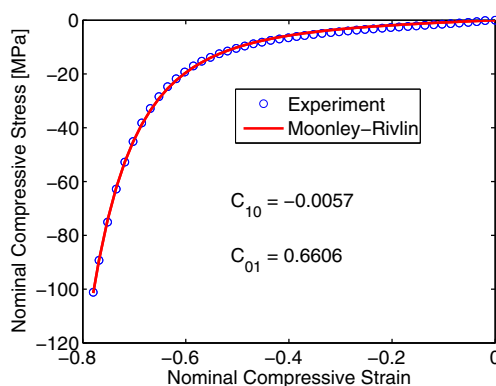


Fig. 5 Nominal compression stress-strain curve for elastic cushion

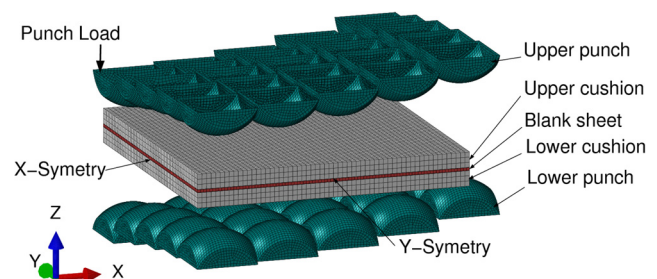


Fig. 6 Finite element model for convex shape

3072 solid elements of the C3D8R type with 4356 nodes. The upper punch was meshed as 27,056 rigid shell elements of the R3D4 type with 4 element nodes, and the total nodes are 28,212. The contact between the sheet blank and the elastic cushion was modeled as surface-to-surface contact. Furthermore, the contact between the elastic cushion and the punch elements was modeled as general contact, which can simplify the contact definition process considerably. The coefficient of friction was set to 0.1 for both contacts.

2.4 Process parameters

Forming process parameters, such as the material properties of the blank, blank thickness, blank cross-section, frictional properties, curvature radius, and punch width have an influence on the performance of multi-curvature forming. The punch pressure (cushion compressive strain ratio), cushion thickness, and punch speed are the most critical design parameters for maintaining wrinkling and dimpling in the multi-point forming apparatus. In this study, we considered two simulation cases. In the first case, as shown in Fig. 7a, a numerical simulation was performed with the parameters of a cushion thickness 10 mm, a punch speed of 100 mm/s, and a compressive strain ratio of 0 % for the elastic cushion; as a result, a compression effect (expected

area of wrinkling) was observed from the maximum principal stress distribution, and wrinkles were also visible in this area. On the contrary, for second case, in which the compressive strain ratio of the elastic cushion was 50 % and the cushion thickness and punch speed were the same as those in case 1, dimples were induced, as shown in Fig. 7b. For both cases, the remaining parameters were as follows: initial blank thickness t_b of 2 mm, punch width P of 40 mm, punch-tip radius r of 30 mm, target curvature radius R of 800 mm, and blank cross-sectional area $L \times W$ of 320 mm \times 320 mm.

The range of the compressive strain ratios of elastic cushion was obtained from the material properties of the cushion. Since the selected material of the elastic cushion was polyurethane with the hardness of Shore 90A with a 55 % compressive strain ratio, the punch can move a maximum of 55 % of the elastic cushion thickness within its elastic range. For this study, we used the cushion compressive strain ratio of 50 % as upper bound. The cushion thickness value and the punch speed range were taken from a previous study [9].

The ranges of the forming process parameters are specified as follows:

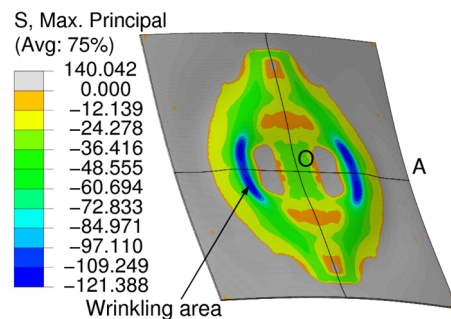
$$\begin{cases} \text{Punch speed} \Rightarrow [50 \leq v \leq 150], \text{ in mm/s} \\ \text{Cushion compressive strain ratio} \Rightarrow [0 \leq c \leq 0.5], \text{ in \%} \\ \text{Cushion thickness} \Rightarrow [4 \leq t_c \leq 16], \text{ in mm} \end{cases}$$

For convenience, the normalized non-dimensional vector of the process parameters $x = [x_1, x_2, x_3]$ are defined as below:

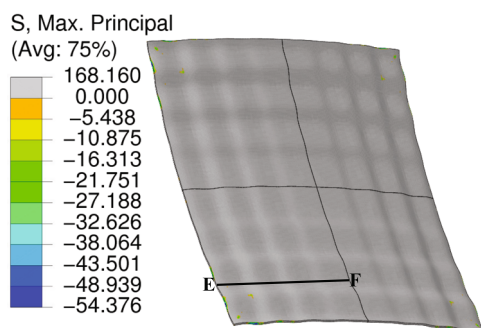
$$x_1 = \frac{v - v^{\min}}{v^{\max} - v^{\min}}, x_2 = \frac{c - c^{\min}}{c^{\max} - c^{\min}}, x_3 = \frac{t_c - t_c^{\min}}{t_c^{\max} - t_c^{\min}}.$$

2.5 Quantification of dimpling

In MPF, dimples are induced because of point contacts between the respective punch ends and the sheet plate. The



(a) Case 1: Cushion compressive strain ratio of 0%, cushion thickness of 10 mm, and punch speed of 100 mm/s



(b) Case 2: Cushion compressive strain ratio of 50%, cushion thickness of 10 mm, and punch speed of 100 mm/s

Fig. 7 Simulation results (only the compression values were considered for the maximum principal stress distributions)



Fig. 8 Multi-point forming apparatus

thickness of the deformed sheet will change significantly by the occurrence of dimples. The root mean square of the thickness deviation for the sheet blank at the integration point from the initial blank thickness is used to evaluate the dimpling effect by FE analysis. The dimpling function is defined by

$$f_d(t) = \sqrt{\frac{1}{N_e} \sum_{i=1}^{N_e} (t_0 - t_f^i)^2}, \quad (5)$$

where N_e is the total number of elements, t_0 is the initial blank thickness, and t_f is the final blank thickness.

2.6 Quantification of wrinkling

A wrinkle is the buckled area of the deformed part. The height of the buckled surface can be evaluated from the curvature difference between the target surface and the deformed surface. For this study, we used the node displacement to evaluate the curvature difference between the target surface and the deformed surface. For the saddle shape, wrinkling is induced only in a few regions and the

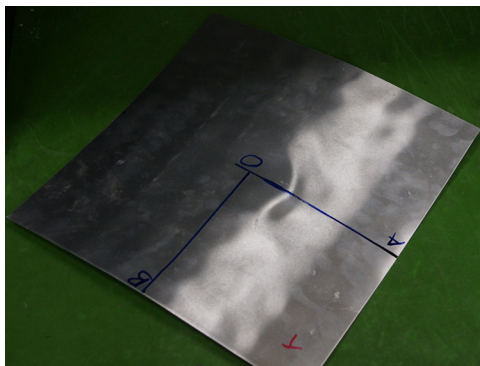
remaining regions remain wrinkle-free. This makes it difficult to observe the difference if the average curvature deviation is to be evaluated. Therefore, wrinkling is evaluated as the maximum curvature difference of the surface. The wrinkling function is defined by

$$f_w(u) = \max_{1 \leq i \leq N} (u^i - u_f^i), \quad (6)$$

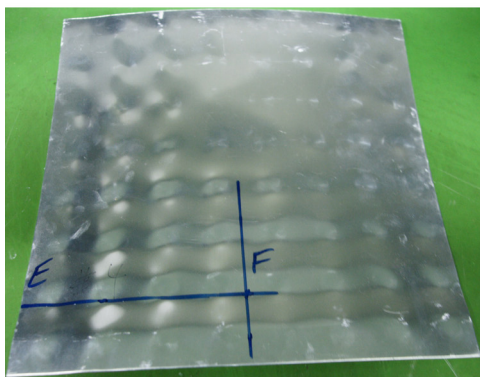
where N is the total number of nodes, u is the node displacement of the target surface, and u_f is the node displacement after deformation.

2.7 Finite element model validation

Before proceeding MPF process optimization, the outcomes of the FE model with respect to the real products are experimentally validated with the two simulation cases described earlier. A multi-curvature forming experiment was performed using the MPF apparatus for the saddle shape, as shown in Fig. 8. The punch width and punch-tip radius employed for the experimental apparatus were the same as those used in the numerical cases. In the first case, 10 mm elastic cushions were used for both sides, and the vertical displacement of the upper punch was controlled until a cushion compression of 0 % was achieved. As shown in Fig. 9a, wrinkling was observed, as was expected from the simulation result shown in Fig. 7a. In the second case, the same cushion thickness and punch speed as those in the first case were employed, and a force of 238 t was applied; this value was established via numerical simulation as the force required for achieving a compression of 50 % of the elastic cushion. As shown in Fig. 9b, dimples were observed, as was also expected from the simulation result shown in Fig. 7b. A three-dimensional scanner was used to measure the surface of the deformed blank in order to compare the numerical simulation results with the experiment results. Figure 10a shows a comparison of curvatures at section AO for case 1 and at section EF for case 2. The



(a) Case 1: Compressive strain ratio of 0% for cushion, cushion thickness of 10 mm, and punch speed of 100 mm/s



(b) Case 2: Compressive strain ratio of 50% for cushion, cushion thickness of 10 mm, and punch speed of 100 mm/s

Fig. 9 Experimental results

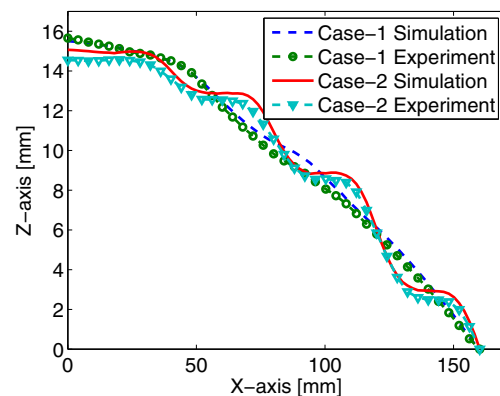


Fig. 10 Experimental and simulation results at section OA for case 1 and at section EF for case 2

root mean square error (RMSE) values of the simulation results with respect to the experimental results are 0.0502 for case 1 and 0.0558 for case 2. This result shows that the simulation results are acceptable with the estimation errors.

3 Kriging surrogate modeling

Both the experimental and the numerical simulation results show that the three parameters have an influence on the defects of dimples and wrinkles in MPF. The next step is to compensate for these defects simultaneously with the help of Kriging surrogate-based optimization. Conducting physical experiments for the entire design space to construct the surrogate model is expensive from the viewpoints of the material, manpower, and time. Therefore, numerical simulations are employed to create the model and verification of the model.

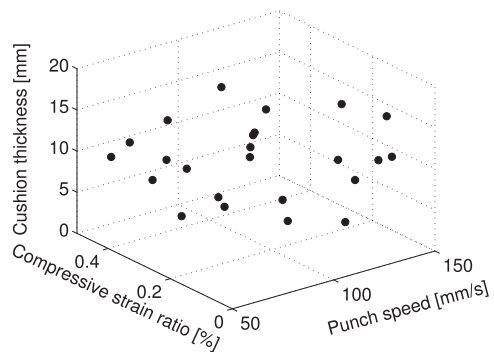
3.1 Sampling strategy

The space-filling Latin hypercube sampling is one of sampling methods for computer experiments, which is intro-

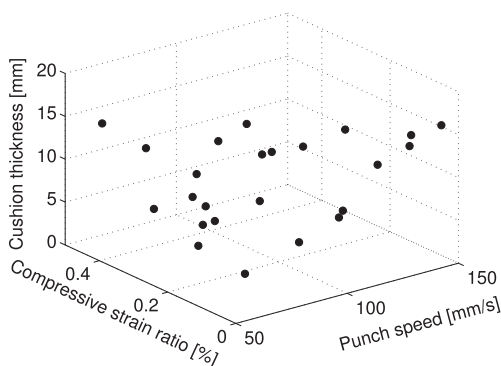
duced by Johnson et al. [22]. The free access MATLAB code [23] was used for this study to obtain 24 training samples. In addition, 24 random samples were generated for verification of the computed surrogate model. Figure 11a, b shows the scatter plots of the training and the random samples. Tables 6 and 7 present the raw data of training and testing, respectively.

3.2 Ordinary Kriging formulation

After the evaluation of the dimpling and wrinkling measures at the Latin hypercube samples, we approximate the functional relationships between the dimpling/wrinkling measures and the three MPF parameters by used ordinary Kriging interpolation [23]. For a setup, let $y \in \mathbb{R}$ be an output of interest, and $\mathbf{x} \in \mathcal{D} \subset \mathbb{R}^k$ be the inputs of y on a domain $\mathcal{D} = \mathbf{x}_l \times \mathbf{x}_u$, where $\mathbf{x}_l \in \mathbb{R}^k$ and $\mathbf{x}_u \in \mathbb{R}^k$ are the lower and upper bounds of \mathbf{x} , respectively. In our application, y indicates either of the two forming defectiveness, such as dimpling f_d and wrinkling f_w , and \mathbf{x} denotes the three MPF parameters, such as a punch speed x_1 , a punch pressure (cushion compressive strain ratio) x_2 , and an elastic cushion thickness x_3 ; hence, $\mathbf{x} = [x_1, x_2, x_3]^T \in \mathbb{R}^3$. Moreover, \mathcal{D} is defined by $\mathbf{x}_l = [50 \text{ mm/s}, 0 \%, 4 \text{ mm}]^T$

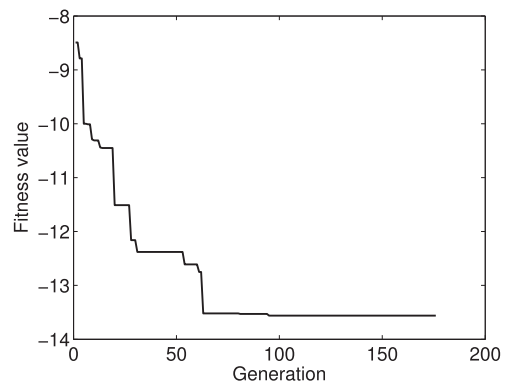


(a) Latin hypercube sampling data for training

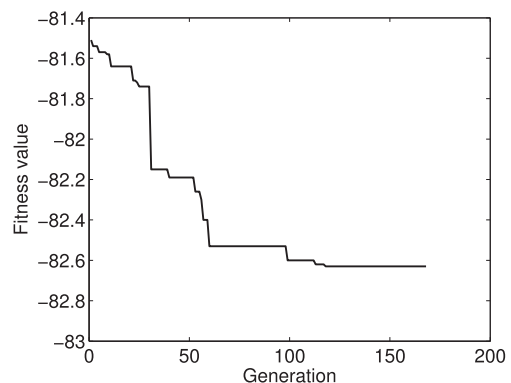


(b) Random sampling data for testing

Fig. 11 Sample data and random data for surrogate modeling



(a) Wrinkling



(b) Dimpling

Fig. 12 History of generations of the best fitness value

and $\mathbf{x}_u = [150 \text{ mm/s}, 0.5 \%, 16 \text{ mm}]^T$. For simplicity, we presume that the dimpling and wrinkling measures are statistically independent so that we can separately construct each Kriging interpolation model of the two forming defectiveness without taking account of their correlation.

To interpolate a set of outputs $\{y_i\}_{i=1}^n$ observed at a set of inputs $\{\mathbf{x}_i\}_{i=1}^n$ from a statistical viewpoint, we regard $y(\mathbf{x})$ as a realization of a random variable $Y(\mathbf{x})$ resulted from a stochastic process $Y : \mathcal{D} \times \Omega \rightarrow \mathbb{R}$, where Ω is a sample space with a probability measure P . For instance, Y becomes an ordinary function $Y_\omega : \mathcal{D} \rightarrow \mathbb{R}$ for an event $\omega \in \Omega$, and on the other hand, Y turns into a random variable $Y(\mathbf{x}) : \Omega \rightarrow \mathbb{R}$ for an input $\mathbf{x} \in \mathcal{D}$. According to the formulation of the Kriging interpolation, y is attributed to a deterministic part $f : \mathcal{D} \rightarrow \mathbb{R}$ and a stochastic part $Z : \mathcal{D} \times \Omega \rightarrow \mathbb{R}$ such that

$$Y(\mathbf{x}, \omega) = f(\mathbf{x}) + Z(\mathbf{x}, \omega), \quad (7)$$

where f represent the global trend of y , and Z stands for the variation of y with respect to f . By the form of $f(\mathbf{x})$, Kriging interpolation techniques go by different names, and here we adopt the ordinary Kriging formulation, which assumes $f(\mathbf{x})$ to be a constant $\mu \in \mathbb{R}$ regardless of \mathbf{x} .

As for Z , we introduce a few assumptions as follows. First, we presume that $Z(\mathbf{x}, \omega)$ is a zero-mean Gaussian stochastic process characterized by a covariance function $\sigma^2 \psi : \mathbb{R}^k \times \mathbb{R}^k \rightarrow \mathbb{R}$, where $\sigma^2 \in \mathbb{R}$ is a process variance, and $\psi : \mathbb{R}^k \times \mathbb{R}^k \rightarrow \mathbb{R}$ is a correlation function. Given a pair of inputs $(\mathbf{x}_i, \mathbf{x}_j)$, ψ is determined by hyperparameters $\boldsymbol{\theta} \in \mathbb{R}^k$ such that $\psi(\mathbf{x}_i, \mathbf{x}_j; \boldsymbol{\theta})$. We further assume that Z is a stationary process by employing ψ invariant to translation in \mathbf{x} such that $\psi(\mathbf{x}_i, \mathbf{x}_j; \boldsymbol{\theta}) = \psi(\mathbf{x}_i - \mathbf{x}_j; \boldsymbol{\theta})$. There are various correlation functions available for Kriging interpolation, and we utilize the popular Gaussian correlation function defined by

$$\begin{aligned} \psi(\mathbf{x}_i, \mathbf{x}_j; \boldsymbol{\theta}) &= \prod_{l=1}^k \exp\left(-\theta_l |x_i^{(l)} - x_j^{(l)}|^2\right) \\ &= \exp\left(-\sum_{l=1}^k \theta_l |x_i^{(l)} - x_j^{(l)}|^2\right), \end{aligned} \quad (8)$$

where $x_i^{(l)}$ and $x_j^{(l)}$ are the l th element of \mathbf{x}_i and \mathbf{x}_j , respectively. Since Z is a Gaussian process, it generates Gaussian random variables $\{Z(\mathbf{x}_i)\}_{i=1}^n \sim \mathcal{N}(\mathbf{0}, \sigma^2 \boldsymbol{\Psi})$, where $\mathbf{0} \in \mathbb{R}^n$ is a zero vector, and $\boldsymbol{\Psi} \in \mathbb{R}^{n \times n}$ is a correlation matrix whose elements depends on $\psi(\mathbf{x}_i, \mathbf{x}_j)$. Because of Z , Y also becomes a Gaussian process producing Gaussian random variables $\{Y(\mathbf{x}_i)\}_{i=1}^n \sim \mathcal{N}(\mu \mathbf{1}, \sigma^2 \boldsymbol{\Psi})$, where $\mathbf{1}$ is a vector of n ones.

3.3 Parameter estimation by maximum likelihood method

As a result of the preceding assumptions, outputs in a vector form $\mathbf{y} = [y_1, \dots, y_n]^T \in \mathbb{R}^n$ follow $\mathcal{N}(\mu \mathbf{1}, \sigma^2 \boldsymbol{\Psi})$ such that

$$\begin{aligned} \pi(\mathbf{y}; \mu, \sigma^2, \boldsymbol{\theta}) &= \frac{1}{(2\pi\sigma^2)^{n/2} |\boldsymbol{\Psi}|^{1/2}} \\ &\times \exp\left(-\frac{1}{2\sigma^2} (\mathbf{y} - \mu \mathbf{1})^T \boldsymbol{\Psi}^{-1} (\mathbf{y} - \mu \mathbf{1})\right), \end{aligned} \quad (9)$$

which is parametrized by μ , σ^2 , and $\boldsymbol{\theta}$. From the probability density function of \mathbf{y} in Eq. 9, we derive a likelihood function \mathcal{L} to infer the three parameters— μ , σ^2 , and $\boldsymbol{\theta}$ —given the outputs \mathbf{y} .

$$\begin{aligned} \mathcal{L}(\mu, \sigma^2, \boldsymbol{\theta}; \mathbf{y}) &= \frac{1}{(2\pi\sigma^2)^{n/2} |\boldsymbol{\Psi}|^{1/2}} \\ &\times \exp\left(-\frac{1}{2\sigma^2} (\mathbf{y} - \mu \mathbf{1})^T \boldsymbol{\Psi}^{-1} (\mathbf{y} - \mu \mathbf{1})\right). \end{aligned} \quad (10)$$

To facilitate parameter estimation by the method of maximum likelihood estimation (MLE), we formulate a log-likelihood function $\ln \mathcal{L}$ such that

$$\begin{aligned} \ln \mathcal{L} &= -\frac{n}{2} \ln(2\pi) - \frac{n}{2} \ln(\sigma^2) \\ &- \frac{1}{2} \ln |\boldsymbol{\Psi}| - \frac{1}{2\sigma^2} (\mathbf{y} - \mu \mathbf{1})^T \boldsymbol{\Psi}^{-1} (\mathbf{y} - \mu \mathbf{1}). \end{aligned} \quad (11)$$

Among the three parameters, we evaluate the maximum likelihood (ML) estimates of μ and σ^2 analytically by annihilating the first derivatives of $\ln \mathcal{L}$ with respect to μ and σ^2 as follows:

$$\begin{aligned} \left. \frac{\partial \ln \mathcal{L}}{\partial \mu} \right|_{\sigma^2, \boldsymbol{\theta}} &= 0 \implies \hat{\mu} = \frac{\mathbf{1}^T \boldsymbol{\Psi}^{-1} \mathbf{y}}{\mathbf{1}^T \boldsymbol{\Psi}^{-1} \mathbf{1}}, \\ \left. \frac{\partial \ln \mathcal{L}}{\partial \sigma^2} \right|_{\mu, \boldsymbol{\theta}} &= 0 \implies \hat{\sigma}^2 = \frac{(\mathbf{y} - \mu \mathbf{1})^T \boldsymbol{\Psi}^{-1} (\mathbf{y} - \mu \mathbf{1})}{n}. \end{aligned} \quad (12)$$

Note that $\hat{\mu}$ in Eq. 12 is the sample mean of \mathbf{y} weighted by $\boldsymbol{\Psi}^{-1}$; If $\boldsymbol{\Psi}^{-1} = \mathbf{I}$, $\hat{\mu}$ boils down to the usual sample mean of \mathbf{y} . Subsequently, we feed the previously evaluated $\hat{\mu}$ and $\hat{\sigma}^2$ into $\ln \mathcal{L}$ for the estimation of $\boldsymbol{\theta}$, which leads to the following concentrated log-likelihood function

$$\ln \mathcal{L}_c \approx -\frac{n}{2} \ln(\hat{\sigma}^2) - \frac{1}{2} \ln |\boldsymbol{\Psi}| \quad (14)$$

after terms that do not involve $\boldsymbol{\theta}$ are dropped. Since the concentrated log-likelihood function in Eq. 14 is a nonlinear function of $\boldsymbol{\theta}$, we resort to nonlinear unconstrained

Table 2 Values of Kriging hyperparameter θ

	Punch speed, $\hat{\theta}_1$	Cushion compressive strain ratio, $\hat{\theta}_2$	Cushion thickness, $\hat{\theta}_3$
Dimpling	12.752	15.793	12.092
Wrinkling	0.471	17.255	8.006

optimization algorithms to find the ML estimate of θ by solving

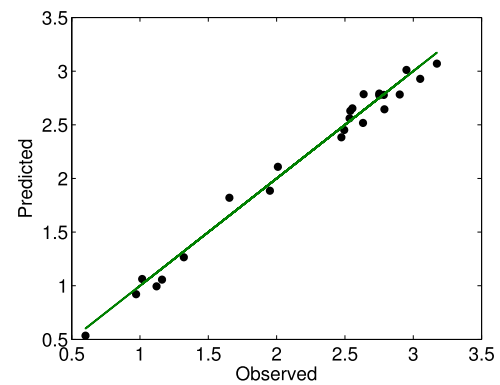
$$\arg \max_{\theta \in \Theta} \ln \mathcal{L}_c(\theta), \quad (15)$$

where $\Theta = \theta_l \times \theta_u \in \mathbb{R}^k$ is the search domain of θ defined by θ_l and θ_u , i.e., the lower and upper bounds of θ , respectively. Note that θ should be nonnegative since ψ is required to satisfy $\psi(\mathbf{0}) = 1$. To address the nonlinear optimization problem in Eq. 15, we capitalize on the genetic algorithm (GA), which is capable of searching for the global optimum, in order not to be trapped in local optima.

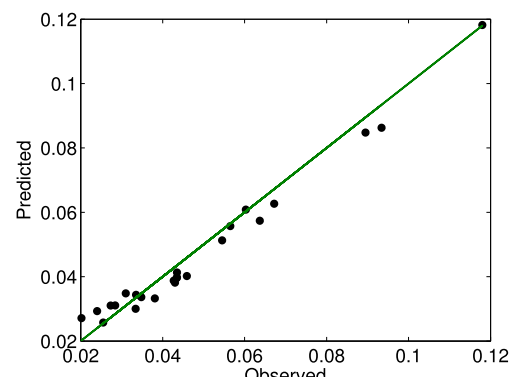
The genetic algorithm works on a population using a set of operators that are applied to the population. A population is a set of design spaces. The generation of the population is computed using the non-dominated rank and a distance measure of the individuals in the current generation; see MATLAB documentation for further details (<http://www.mathworks.com/help/gads/multiobjective-optimization.html>). In this study, we used a population size of 100 and maximum number of generations as 300. Figure 12a, b shows the history of a generations of the fitness value for wrinkling and dimpling, respectively, until GA converges to the best value. The optimization is terminated before it reaches the given maximum number of generation for both wrinkling and dimpling. This shows that the given maximum number of generation is an adequate number. The initial upper and lower bounds for search of $\log_{10}(\theta)$ are 3 and -3 respectively. If the ML estimate $\hat{\theta}$ value corresponding to a variable is high, the corresponding variable has great influence than the other variables. As seen from Table 2, both wrinkling and dimpling are more dependent on the cushion compressive strain ratio (punch pressure). The Punch speed has a smaller effect on wrinkling than the other parameters.

Table 3 Results of model verification

	Data	R^2	RMSE	NRMSE
Dimpling	Training	1.0	2.38×10^{-18}	1.85×10^{-17}
	Testing	0.9701	8.32×10^{-4}	8.50×10^{-3}
Wrinkling	Training	1.0	4.14×10^{-16}	1.60×10^{-16}
	Training	0.9847	9.39×10^{-2}	3.65×10^{-2}



(a) Wrinkling



(b) Dimpling

Fig. 13 Observed results vs. predicted results

3.4 Prediction by maximum likelihood method

Once we evaluate the ML estimates, we make a prediction at an unseen input $x_0 \in \mathcal{D} \subset \mathbb{R}^k$ and $x_0 \notin \{x_i\}_{i=1}^n$ by treating $y_0 = y(x_0) \in \mathbb{R}$ as a realization of a random variable $Y(x_0)$ from the Gaussian process Y , from which y stemmed. Thus, augmented outputs $\tilde{y} = [y; y_0] \in \mathbb{R}^{n+1}$ are realizations of Gaussian random variables $\{Y(x_i)\}_{i=1}^{n+1} \sim \mathcal{N}(\mu \mathbf{1}, \sigma^2 \Psi)$, where $\mathbf{1}$ is a vector of $n+1$ ones, and

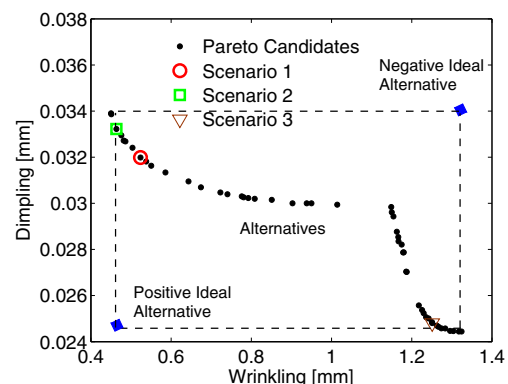
**Fig. 14** Pareto fronts for minimizing dimpling and wrinkling

Table 4 TOPSIS results for different weights of dimpling and wrinkling

Scenario	Weight		TOPSIS result	
	Dimpling	Wrinkling	Dimpling (mm)	Wrinkling (mm)
1	0.5	0.5	0.0320	0.524
2	0.25	0.75	0.0332	0.467
3	0.75	0.25	0.0248	1.251

$\tilde{\Psi} \in \mathbb{R}^{(n+1) \times (n+1)}$ is an augmented correlation matrix with $\{\mathbf{x}_i\}_{i=1}^{n+1} = \{x_1, \dots, x_n, x_0\}$ such that

$$\tilde{\Psi} = \begin{bmatrix} \Psi & \psi \\ \psi^T & 1 \end{bmatrix}. \quad (16)$$

Here, $\psi = [\psi(x_1, x_0), \dots, \psi(x_n, x_0)]^T \in \mathbb{R}^n$ is a vector of correlations between the previous inputs $\{x_i\}_{i=1}^n$, at which outputs \mathbf{y} are known, and the new input x_0 , at which an output y_0 is unknown. Similar to the preceding parameter estimation, we formulate a log-likelihood function based on the probability density function of $\tilde{\mathbf{y}}$ as below

$$\ln \tilde{\mathcal{L}} = -\frac{n}{2} \ln(2\pi) - \frac{n}{2} \ln(\hat{\sigma}^2) - \frac{1}{2} \ln |\tilde{\Psi}| - \frac{1}{2\hat{\sigma}^2} (\tilde{\mathbf{y}} - \hat{\mu}\mathbf{1})^T \tilde{\Psi}^{-1} (\tilde{\mathbf{y}} - \hat{\mu}\mathbf{1}), \quad (17)$$

and reduce it to the following log-likelihood function

$$\begin{aligned} \ln \tilde{\mathcal{L}} &\approx -\frac{1}{2\hat{\sigma}^2} (\tilde{\mathbf{y}} - \hat{\mu}\mathbf{1})^T \tilde{\Psi}^{-1} (\tilde{\mathbf{y}} - \hat{\mu}\mathbf{1}) \\ &= -\frac{1}{2\hat{\sigma}^2} \begin{bmatrix} \mathbf{y} - \hat{\mu}\mathbf{1} \\ y_0 - \hat{\mu} \end{bmatrix}^T \begin{bmatrix} \Psi & \psi \\ \psi^T & 1 \end{bmatrix}^{-1} \begin{bmatrix} \mathbf{y} - \hat{\mu}\mathbf{1} \\ y_0 - \hat{\mu} \end{bmatrix} \end{aligned} \quad (18)$$

by leaving out terms irrelevant to y_0 . By exploiting the partitioned inverse method [24], we can analytically evaluate

$\tilde{\Psi}^{-1}$ in terms of Ψ and ψ , which helps us reshape the log-likelihood function as

$$\begin{aligned} \ln \tilde{\mathcal{L}} &\approx -\left(\frac{1}{2\hat{\sigma}^2 (1 - \psi^T \Psi^{-1} \psi)} \right) (y_0 - \hat{\mu})^2 \\ &\quad + \left(\frac{\psi^T \Psi^{-1} (\mathbf{y} - \hat{\mu}\mathbf{1})}{\hat{\sigma}^2 (1 - \psi^T \Psi^{-1} \psi)} \right) (y_0 - \hat{\mu}). \end{aligned} \quad (19)$$

Finally, we evaluate the ML estimate of y_0 as follows:

$$\frac{\partial \ln \tilde{\mathcal{L}}}{\partial y_0} = 0 \implies \hat{y}_0(x_0) = \hat{\mu} + \psi^T \Psi^{-1} (\mathbf{y} - \hat{\mu}\mathbf{1}). \quad (20)$$

The above equation conveys that a μ -shifted output $\hat{y}_0 - \hat{\mu}$ can be predicted as a linear combination of a basis ψ and coefficients $\Psi^{-1}(\mathbf{y} - \hat{\mu}\mathbf{1})$.

3.5 Verification of Kriging model

To ensure that the approximation model is sufficiently accurate, we evaluate numerical metrics such as root mean square error (RMSE), normalized root mean square error (NRMSE), and coefficient of determination (R^2).

RMSE is given as

$$\text{RMSE} = \sqrt{\frac{1}{n} \sum_{i=1}^n (\hat{y}_i(x) - y_i(x))^2},$$

where n is the number of sample points, $y(x)$ is the actual value, and $\hat{y}(x)$ is the predicted value.

NRMSE is defined as

$$\text{NRMSE} = \frac{\text{RMSE}}{(y_{\max} - y_{\min})},$$

where y_{\max} and y_{\min} is the maximum and minimum actual value, respectively.

R^2 is formulated as

$$R^2 = 1 - \frac{SS_{\text{res}}}{SS_{\text{tot}}},$$

here, SS_{tot} is the total sum of squares (proportional to the variance of the data)

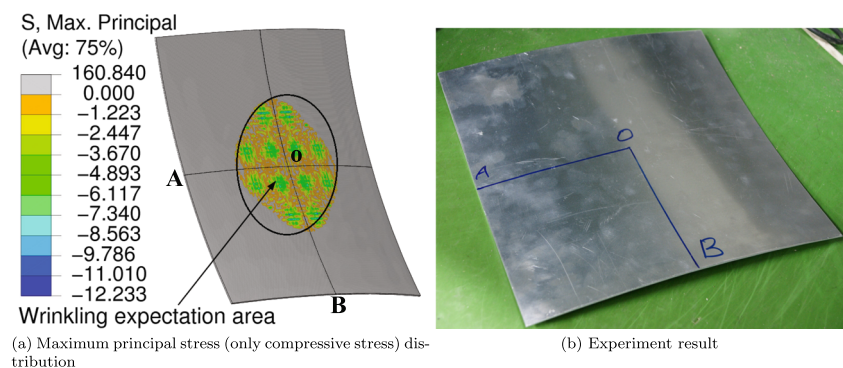
Fig. 15 Optimized result for scenario 1

Table 5 Verification of Kriging prediction with simulation result for scenario 1

	Punch speed (mm/s)	Cushion compressive strain ratio (%)	Cushion thickness (mm)	Dimpling (mm)	Wrinkling (mm)
Kriging prediction	128.8	6.35	15.87	0.0320	0.524
Full model simulation	128.8	6.35	16	0.0331	0.527
Relative error (%)				3.32	−5.69

$$SS_{tot} = \sum_i [y_i(x) - \bar{y}]^2,$$

where \bar{y} is the mean of the observed data, and $y_i = (y_1, y_2, \dots, y_n)$. SS_{res} is the sum of squares of residuals, which is also termed the residual sum of squares:

$$SS_{res} = \sum_i [y_i(x) - \hat{y}_i(x)]^2,$$

where y_i is the actual value (y_1, y_2, \dots, y_n), \hat{y}_i is the predicted value ($\hat{y}_1, \hat{y}_2, \dots, \hat{y}_n$).

Table 3 summarizes model verification with R^2 , RMSE, and NRMSE values for training and testing data. Verification results for both these sets of data show that the Kriging interpolation model well predicts the observed data. Figure 13a, b shows the prediction results of the model in comparison to the observed results. From the figures, it is clear that both training and testing samples are clustered around the straight line, which implies that the predicted responses by the model are quite close to the observed responses.

4 Multi-objective process optimization

4.1 Optimization formulation

In this study, the multi-objective function is constructed based on the two formability criteria. As mentioned in Section 2, the element thickness on the stamping part is used to evaluate the dimpling effect. The curvature radius difference between the target shape and the deformed shape

is used to examine the wrinkling effect. The formulation is given as

$$\begin{aligned} \min & (f_d(x), f_w(x)) \\ \text{s.t.} & 0 \leq x_i \leq 1, \end{aligned} \quad (21)$$

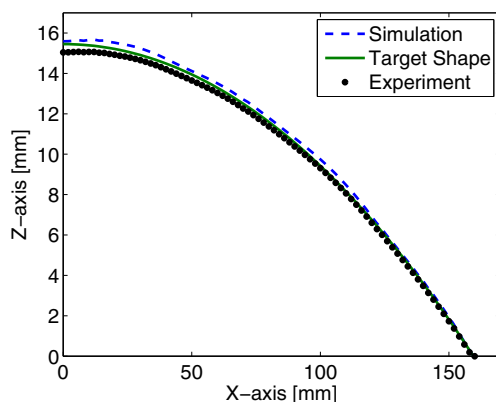
where, $x_i = (x_1, x_2, x_3)$ is the process parameter, the first objective is to minimize the average thickness deviation at the integration point from the initial thickness of the sheet blank. The second objective is to minimize the maximum curvature deviation from the target curvature radius.

4.2 Results and discussion

In this study, the multi-objective genetic algorithm was employed to obtain the Pareto front of the two objective functions. The Pareto fraction and distance function are used to control the elitism of the genetic algorithm. The Pareto fraction option limits the number of individuals on the Pareto front, and the distance function helps maintain diversity on a front by favoring individuals that are relatively far away from the front. We used a population size of 100, and a Pareto fraction of 0.5 (50 % of the population size), and 300 generations.

To decide the best combination, we applied TOPSIS, a widely used decision-making method introduced by Hwang et al. [25]. TOPSIS is used to select the alternative that has the shortest Euclidean distance to the positive ideal solution and the farthest Euclidean distance from the negative ideal solution. A positive ideal solution is that which has the best level for all attributes considered, whereas the negative ideal solution is that which has the worst attribute values; for more developed methods, see the book of Tzeng and Huang [26]. Figure 14 shows the candidates of the Pareto front and TOPSIS results at different weights of the dimpling and wrinkling. Table 4 summarizes the weight values.

Computer simulation was performed using the obtained forming parameter values in scenario 1 described in Table 4. As shown in Fig. 15a, the dimpling-and-wrinkling free result was examined using numerical simulation results. The maximum curvature deviation obtained from the simulation result was 0.0527 mm, and the average thickness was 0.0331 mm. As clear shown in Table 5, the results of the predicted model are quite similar to the simulation results with the relative errors for dimpling and wrinkling being 3.32 and −5.69 % respectively.

**Fig. 16** Curvature for optimized result at section OA

For validation, a multi-curvature forming experiment was then performed by adopting the optimized parameters of a punch speed of 128.8 mm/s, elastic cushion thickness of 16 mm, and force of 33.5 t. The force value was obtained from simulation result for an elastic cushion compression of 6.35 %. As shown in Fig. 15b, the experimental results agreed well with the simulation results, and the experimental results were also both wrinkling and dimpling free. Figure 16 shows the curvature difference at section AO as obtained from the experiment (via a 3D scanner) with the simulation result and the target shape. The RMSE between the experimental and simulation results is 0.0505, and that between the experimental result and the target shape is 0.0264. Both of these errors are fairly acceptable.

Finally, we investigate the computational efficiency of the Kriging surrogate model. The computer we used had the following specifications: Window 7 Operating System (64-bit), Intel (R) Core (TM) i5-4,670 CPU @3.40 GHz processor, 16.0 GB installed memory (RAM). An average time of 6763 s (1.88 h) was required for generating one numerical simulation result. To construct the Kriging model, we used 24 training samples and 24 testing samples. GA optimization calls 12,001 functions to converge towards the Pareto front. This means, if we used FE model without Kriging surrogate model, it would take 22,561.88 h ($12,001 \times 1.88$ h). However, using Kriging surrogate model saved 22,471.64 h ($(12,001 - 48) \times 1.88$ h), this demonstrates how the computational efficiency of the Kriging surrogate model method is.

5 Conclusions

This research investigates the MPF process by constructing a Kriging surrogate model to reduce wrinkling and dimpling defects. The multi-objective genetic algorithm has been employed to obtain the Pareto front for compensating both wrinkling and dimpling. TOPSIS was also applied to establish the best parameter combination from among the candidates of the Pareto front, and a wrinkling-and-dimpling-free result was thus obtained by TOPSIS.

From Kriging hyperparameter result, this study conclude that wrinkling and dimpling are more dependent on punch pressure, and the punch speed has less effect for wrinkling than the other process parameters. Verification results of the surrogate model also demonstrated its ability to handle multi-objective optimization of expensive functions for the MPF application. The proposed Kriging surrogate model is expected to predict any complicated sheet metal forming process while saving computational time.

Acknowledgments This work was supported by the National Research Foundation of Korea (NRF) grant funded by the Korea government (MSIP) (No. 2012R1A5A1048294).

Appendix: Experimental designs

Table 6 Latin hypercube design for training

Case	Punch speed, x_1	Cushion compression ratio, x_2	Cushion thickness, x_3
1	141.30	0.20	5.57
2	119.60	0.09	4.00
3	71.70	0.35	14.96
4	150.00	0.30	12.35
5	93.50	0.43	6.09
6	50.00	0.39	11.30
7	115.20	0.46	13.91
8	145.70	0.11	9.74
9	80.40	0.02	8.18
10	123.90	0.41	8.70
11	89.10	0.28	4.52
12	102.20	0.00	14.43
13	76.10	0.50	9.22
14	137.00	0.07	16.00
15	54.40	0.24	13.40
16	58.70	0.22	6.62
17	67.40	0.37	7.65
18	63.00	0.13	10.26
19	132.60	0.48	5.04
20	110.90	0.33	10.78
21	106.50	0.26	15.48
22	128.30	0.04	11.84
23	84.80	0.17	12.87
24	97.80	0.15	7.13

Table 7 Random design for testing

Case	Punch speed, x_1	Cushion compression ratio, x_2	Cushion thickness, x_3
1	136.60	0.18	8.80
2	92.70	0.14	5.72
3	85.90	0.23	7.92
4	131.40	0.05	15.18
5	65.20	0.41	4.19
6	119.10	0.11	7.05
7	92.60	0.32	9.56
8	57.90	0.11	13.23
9	78.50	0.26	5.06
10	80.80	0.45	9.84
11	50.80	0.07	5.44

Table 7 (continued)

Case	Punch speed, x_1	Cushion compression ratio, x_2	Cushion thickness, x_3
12	106.60	0.27	5.66
13	110.90	0.41	4.01
14	140.10	0.37	7.74
15	104.80	0.42	15.33
16	63.50	0.03	4.64
17	104.50	0.21	6.44
18	83.00	0.20	12.86
19	74.10	0.03	14.33
20	134.20	0.32	9.58
21	146.40	0.42	9.60
22	106.00	0.19	13.64
23	137.50	0.49	9.02
24	89.60	0.01	8.82

References

- Nakajima N (1969) A newly developed technique to fabricate complicated dies and electrodes with wires. *Journals of Japan Society of Mechanical Engineers* 12:1546–1554
- Valjavec M, Hardt DE (1999) Closed-loop shape control of the stretch forming process over a reconfigurable tool: precision air-frame skin fabrication. *Proceedings of the ASME Manufacturing Engineering Division* 10:909–919
- Park JW, Kim J, Kim KH, Kang BS (2014) Numerical and experimental study of stretching effect on flexible forming technology. *Int J Adv Manuf Technol* 73:1273–1280
- Li M, Nakamura H, Watanabe S (1992) Study of the basic forming principles (1st Report: Research on multi-point forming for sheet metal). In: *Proceedings of the Japanese spring conference for technology of plasticity*, pp 519–522
- Zhongyi C, Mingzhe L (2001) Optimum path forming technique for sheet metal and its realization in multi-point forming. *J Mater Process Technol* 110:136–141
- Heo SH, Seo YH, Park JW, Ku TW, Kim J, Kang BS (2010) Application of flexible forming process to hull structure forming. *J Mech Sci Technol* 24:137–140
- Hui S, Zhong W, Ming YC, Zhe L, Lan YW (2010) Numerical analysis of the multi-point stretch forming process of aircraft outer skin part. *Adv Mater Res* 154–155:1068–1072
- Kim JB, Tang DY (2003) Prediction of wrinkling initiation in sheet metal forming process. *Eng Comput* 20:6–39
- Li MZ, Cai ZY, Sui Z, Yan QG (2002) Multi point forming technology for sheet metal. *J Mater Process Technol* 129:333–338
- Quan GZ, Ku TW, Kang BS (2011) Improvement of formability for multi-point bending process of AZ31B sheet metal using elastic cushion. *Int J Precis Eng Manuf* 12:1023–100
- Cai ZY, Hui S, Li MZ (2008) Numerical investigation of multi point forming process for sheet metal: wrinkling, dimpling and springback. *Int J Adv Manuf Technol* 37:927–936
- Zhang Q, Dean TA, Wang ZR (2006) Numerical simulation of deformation in multi-point sandwich forming. *Int J Mach Tools Manuf* 46:699–707
- Liu Q, Lub C, Fu W, Tieu K, Li MZ, Gongc X (2012) Optimization of cushion conditions in micro multi-point sheet forming. *J Mater Process Technol* 212:672–677
- Wessing S, Rudolph G, Turk S, Klimmek C, Christian S, Schneider M, Lehmann U (2014) Replacing FEA for sheet metal forming by surrogate modeling. *Cogent Engineering*. doi:10.1080/23311916.2014.950853
- Sun G, Li G, Gong Z, He G, Li Q (2011) Radial basis functional model for multi-objective sheet metal forming optimization. *Eng Optim* 43:1351–1366
- Xia W, Yang H, Liao XP, Zeng JM (2014) A multi-objective optimization method based on Gaussian process simultaneous modeling for quality control in sheet metal forming. *Int J Adv Manuf Technol* 72:1333–1346
- Hu W, Enying L, Li GY, Zhong ZH (2007) Optimization of sheet metal forming processes by the use of space mapping based metamodeling method. *Int J Adv Manuf Technol*. doi:10.1007/s00170-007-1253-z
- Kitayama S, Kita K, Yamazaki K (2012) Optimization of variable blank holder force trajectory by sequential approximate optimization with RBF network. *Int J Adv Manuf Technol* 61:1067–1083
- Guo TQ, Batoz JL, Naceur H, Bouabdellah H, Mercier F, Barlet O (2000) Recent developments on the analysis and optimum design of sheet metal forming parts using a simplified inverse approach. *Comput Struct* 78:133–148
- Ingarao G, Di Lorenzo R (2013) A contribution on the optimization strategies based on moving least squares approximation for sheet metal forming design. *Int J Adv Manuf Technol* 64:411–425
- Heo SC, Seo YH, Noh HG, Ku TW, Kang BS (2010) Numerical study on effect of using elastic pads in flexible forming process. *Trans Korean Soc Mech Eng A* 34:549–556
- Johnson ME, Moore LM, Ylvisaker D (1990) Minimax and maximin distance designs. *Journal of Statistical Planning and Inference* 26:131–148
- Forrester A, Sobester A, Keane AJ (2008) *Engineering design via surrogate modeling—a practical guide*. Wiley, University of Southampton
- Thiel H (1971) *Principles of econometrics*. Wiley, New York
- Hwang C-L, Yoon K (1981) *Multiple attribute decision making: methods and applications*. Springer, Berlin
- Tzeng GH, Huang JJ (2011) *Multiple Attribute Decision Making, Methods and applications*. CRC Press Taylor & Francis Group, pp 69–72